Journal of Alloys and Compounds 723 (2017) 689–697

Contents lists available at ScienceDirect

Journal of Alloys and Compounds

journal homepage: http://www.elsevier.com/locate/jalcom

Formation of metastable phases of ferrous sulfide via pulsed Nd:YAG laser deposition: Experimental and theoretical study

Tomáš Křenek [a, *], Rostislav Medlín [a], Stefan Karatodorov [b], Valentin Mihailov [b], Michal Pola [a], A.H. Reshak [a, c]

[a] New Technologies - Research Centre, University of West Bohemia, Univerzitni 8, 306 14 Pilsen, Czech Republic
[b] Georgi Nadjakov Institute of Solid State Physics, Bulgarian Academy of Sciences, 72 Tzarigradsko Chaussee, 1784 Sofia, Bulgaria
[c] School of Material Engineering, University Malaysia Perlis, 01007 Kangar, Perlis, Malaysia

ARTICLE INFO

Article history:
Received 16 May 2017
Accepted 21 June 2017
Available online 24 June 2017

Keywords:
Laser ablation
Ferrous sulfide
Metastable phases
Smythite
Marcasite
Nanostructures

ABSTRACT

Highly polymorphic ferrous sulfide exhibits attractive optical, semiconducting, magnetic and biocatalytic properties related to its phase modification. Nd:YAG laser ablation of ferrous sulfide (FeS) in vaccum results in noncongruent deposition of nanostructured FeS_{1-x} thin films. Deposits have been carried out on Ta, Al and Cu substrates and achieved thin films were analyzed using scanning electron microscopy (SEM), high resolution transmission electron microscopy (HRTEM) and electron diffraction in order to characterize morphology, chemical composition and phase transformation induced by ablative process. Round-shaped and ring-like particles, shapeless agglomerates as well as flat discontinuous areas have been observed for all the coats deposited on various substrates. However, using HRTEM, in agreement with electron diffraction, different phase compositions on various substrates have been detected. Cubic pyrite phase (FeS_2) has been detected on Ta substrate. Metastable rhombohedral smythite Fe_9S_{11} and cubic pyrite FeS_2 have been found on Al substrate. And cubic pyrite FeS_2, metastable rhombohedral smythite Fe_9S_{11} and metastable orthorhombic marcasite FeS_{2m} have been revealed on Cu substrate. The detected crystalline nanograins in all deposits were surrounded by amorphous phase. Furthermore, to gain deep insight into the electronic structure of obtained stable (cubic pyrite) and less known unstable phases (orthorhombic marcasite and rhombohedral smythite) the density functional theory is employed and important characteristics such as band gap values have been calculated.

© 2017 Elsevier B.V. All rights reserved.

1. Introduction

Ferrous sulfide represents an attractive material for solar cell application (eg. [1]) which exhibits also interesting semiconducting eg. [2] and magnetic eg. [3] and biocatalytic eg. [40] properties.

Other solar cell materials such as cadmium lead, indium or selenium possess higher efficiencies, however FeS offers abundance, non-toxicity and low price.

The iron sulfide (FeS) is highly polymorphic system with complex phase diagram containing seven phases: pyrite (cubic- FeS_2), marcasite (calcium chloride structure-FeS_2), pyrrhotite-IT ($Fe_{1-x}S$), pyrrhotite-4M (Fe_7S_8), Fe_9S_{10}, greigite (cubic spinel- Fe_3S_4), troilite-2H (FeS) and mackinawite ($Fe_{1+x}S$) [4–7]. Except stable pyrite (FeS_{2p}) and pyrrhotite (Fe_{1-x}) phases are metastable or unstable. Pyrite phase of iron sulfide is developed for potential application as an absorber material for thin film solar cells due to its band gap (Eg = 0.95 eV) and high absorption coefficient (~10^5 cm^{-1}) [8]. FeS stoichiometric iron sulfide possesses the trollite structure which exhibits antiferromagnetic properties at room temperature. Above 120 °C, trollite transforms to the NiAs-type structure consisting of ($Fe_{1-x}S$) and Fe_7S_8 pyrrhotites [9]. Vacancies of Fe cause that many pyrrhotites ($Fe_{1-x}S$) create compositions with interesting magnetic and electrical properties [10,11]. Fe_xS samples with x = 0.87–0.88 are ferromagnetic Weiss types. The non-stoichiometric $Fe_{1-x}S$ shows different morphologies, including nanorods [12], whiskers [13], and U-shaped microslots [14].

Thin films of iron sulfide have been prepared using ion beam and reactive sputtering [15], vacuum thermal evaporation [16], chemical spray pyrolysis [17], sulfurization of iron oxides [18,19], plasma assisted sulfurization of iron [20], atmospheric-or low-pressure metal–organic chemical vapor deposition (CVD) (eg. ref.

* Corresponding author.
E-mail address: tkrenek@ntc.zcu.cz (T. Křenek).

http://dx.doi.org/10.1016/j.jallcom.2017.06.229
0925-8388/© 2017 Elsevier B.V. All rights reserved.

[21]), laser-CVD of iron pentacarbonyl [$Fe(CO)_5$] hydrogen sulfide and *tetra*-butyl sulfide as precursors [22], flash evaporation [23] and vapor transport [24].

Nanoparticles of iron sulfide have been obtained via high-energy mechanical milling [25].

The laser ablative deposition is a challenging method for preparation of smooth and nanostructured films as well as nanosized particles from elemental, inorganic and organic bulk materials (e.g. refs. [26,27]). There is a lack of information about pulsed laser deposition of iron sulfide and interaction of ablated particles with unheated substrate surface and only a few studies have been published. The laser ablation of pyrite (FeS_2) on aluminium and silica substrates leads to the deposition of films containing FeS constituents under both higher and room temperature [28].

Recently we have published the pulsed IR laser ablative deposition of ferrous sulfide FeS on unheated silica, tantalum and copper substrates [29] and revealed that this process leads to deposition of amorphous S-deficient (FeS_{1-x}) films containing nanosized FeS particles and to reactive deposition on the copper surface. Herein we continue our studies by reporting on near-IR Nd:YAG pulsed laser ablation of FeS and showing that the room-temperature deposition on unheated Al, Ta, Cu substrates allows the formation of different nanocrystalline iron sulfides whose phase composition is affected by the used substrate.

2. Methodology

2.1. Experimental

The near IR laser irradiation and deposition experiments were conducted in 10^{-2} Torr vacuum in a metal reactor with 343 mL volume. A simple experimental setup scheme is given in Fig. 1. The metal reactor had three borosilicate glass windows and it was connected to the vacuum manifold and pressure transducer. The vacuum system used is Lavat AV 63.

For the deposition, we used a pulsed Nd:YAG Quanta Ray GCR3 laser. The pulse duration at 1064 nm was 8 ns and the pulse energies used were up to 165 mJ. The repetition frequency was set to the maximum value of 20 Hz and the number of pulses for each sample was 2500. The radiation was focused with a 25 cm focal distance glass lens, producing up to 600 Jcm^{-2} energy fluence at the target surface. The target was a FeS pellet with diameter 8 mm and height 5 mm positioned in the center of the reactor. The substrate (tantalum, aluminium or copper foils) was positioned vertically above the target on top of a 9.5 cm diameter glass cylinder and was pierced in the middle to allow the passing of the laser beam. For each sample deposition, the vacuum chamber was first opened and the clean substrate placed on top of the glass cylinder. Then, the chamber was closed and the pressure lowered to around 10^{-2} Torr. Thereafter, the laser irradiation by 2500 pulses at the set energy fluence was accomplished. After the irradiation, the pressure was increased up to atmospheric, the chamber was opened and the coated sample taken for examination was replaced with a new substrate.

Transmission electron microscopy (TEM) analysis (particle size and phase analysis) was carried out with a Transmission Electron Microscope JEM 2200FS (Shottky) from JEOL operated at 200 kV with CCD Gatan (Digital Micrograph software), in-column Omega energy filter for EFTEM and EELS analysis, STEM mode with HAADF detector and EDS 80 mm^2 [2] SDD (Silicon Drift Detector) X-Max detector from Oxford on scraped samples that were subsequently dispersed in ethanol followed by the application of a drop of diluted suspension on a polymer/carbon coated Cu grid. The diffraction patterns were evaluated using the database JCPDS-2 and Process Diffraction software package [30]. Scanning Electron Microscope (SEM) analysis was carried out with a JEOL JSM 7600F auto emission microscope with EPMA 50 mm^2 [2] SDD X-MAX EDS.

The FeS pellet was made at 100 atm. on a hydraulic press from a commercially available iron sulfide powder (FeS, 99% Fe, Aldrich).

2.2. Theoretical approach

A step forward to understand the electronic structure of the thin film of FeS_2, the density functional theory (DFT) is utilized. FeS_2 crystallizes in cubic (Pa-3) with two formula units in a unit cell and orthorhombic (*Pnnm*) phases with four formula units in a unit cell. Whereas the smythite Fe_9S_{11} crystallizes in rhombohedral (R-3m) symmetry. The experimental crystallographic data are used as input data for the geometrical relaxation of the atoms in the unit cell. The geometrical relaxation is achieved using the all-electrons full-potential linear augmented plane wave (FPLAPW + lo) method as embodied in the Wien2k code [31] within Perdew-Burke-Ernzerhof generalized gradient approximation (PBE-GGA) [32]. Fig. 2 illustrates the crystal structure of the relaxed geometry for cubic- FeS_2, orthorhombic-FeS_2, and smythite Fe_9S_{11}. The octahedron (FeS_6) is formed by the coordination of Fe with six S atoms. Each Fe atom is surrounded by six S atoms. The octahedrons are joined together through corner-sharing of an S atom. It has been noticed that on going from the cubic phase to the orthorhombic phase the orientation of the net local dipole moment direction of the octahedron changes to the opposite direction (Fig. 2).

Using the obtained relaxed geometry, the electronic band structure, density of states and the electronic charge distribution are calculated using the FPLAPW + lo within the modified Becke-Johnson potential (mBJ) to treat the exchange correlation [33]. The mBJ is a local approximation to an atomic "exact-exchange" potential and a screening term which allows the calculation of band gaps with accuracy similar to the expensive GW calculations [33]. For cubic- FeS_2 (orthorhombic-FeS_2) the muffin-tin radii (R_{MT}) of the Fe and S atoms were chosen in such a way that the spheres did not overlap. The value of R_{MT} is taken to be 2.2 a.u. (2.08 a.u.) for Fe and 1.82 a.u. (1.7 a.u.) for S. While for the smythite Fe_9S_{11} the R'_{MTs} are chosen to be 1.9 and 2.32 a.u. for S and F, respectively.

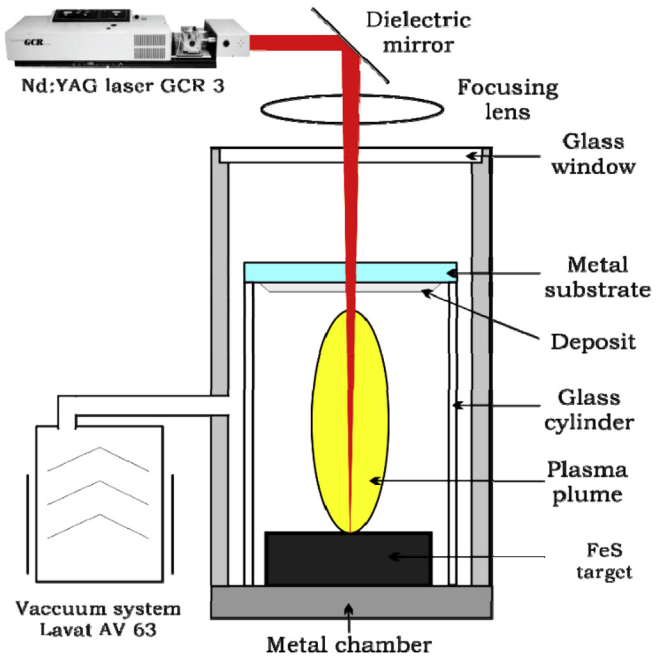

Fig. 1. Scheme of laser ablative deposition.

To achieve the total energy convergence, the basis functions in the interstitial region (IR) were expanded up to $R_{MT} \times K_{max} = 7.0$. The maximum value of l was taken as $l_{max} = 10$, while the charge density is Fourier expanded up to $G_{max} = 12$ (a.u)$^{-1}$. Self-consistency is obtained using 1000 k points in the irreducible Brillouin zone (IBZ). The self-consistent calculations are converged when the total energy of the system is stable within 0.00001 Ry. The ground state properties calculations are performed within 6000 k points in the IBZ.

3. Results and discussion

3.1. Laser deposition

The pulsed laser near-IR (wavelength 1604 nm) irradiation focused on the surface of iron sulfide pellet results in ablation and generation of visible plasma luminescence zone recognizable as a bluish spark filling completely whole space of the reactor. Moreover, laser irradiation causes creation of the crater by vaporized particles which are condensing on Ta, Al and Cu surfaces as solid thin films. The deposits on Al, Ta and Cu possess very similar homogenous metallic like, dark adhesive appearances. The SEM analyses (Fig. 3) of the coats deposited on Al (Fig. 3 A, B), Cu (Fig. 3 C, D) and Ta (Fig. 3 E, F) exhibit morphology consisting of round-shaped particles with size varying from tens of nm up to units of μm on the flat discontinuous areas.

The deposits contain also interesting ring-like particles with tens of nm in diameter as well as shapeless agglomerates. Morphology of the deposit reflects plasma-induced agglomerates and ejected liquid droplets which are rapidly cooled on the unheated substrate. These spherical particles may give rise to amorphous/metastable state. The droplets quenched on the surface are also seen as trailed shaped entities in the film. We also note that the deposit on Cu substrates possesses more nm-sized particles in comparison with deposits on Al and Ta coats.

Similar chemical composition for all three deposits has been confirmed by EDX analyses. Morphological elements of spherical particles, ring-like objects and of flat areas show S-deficient

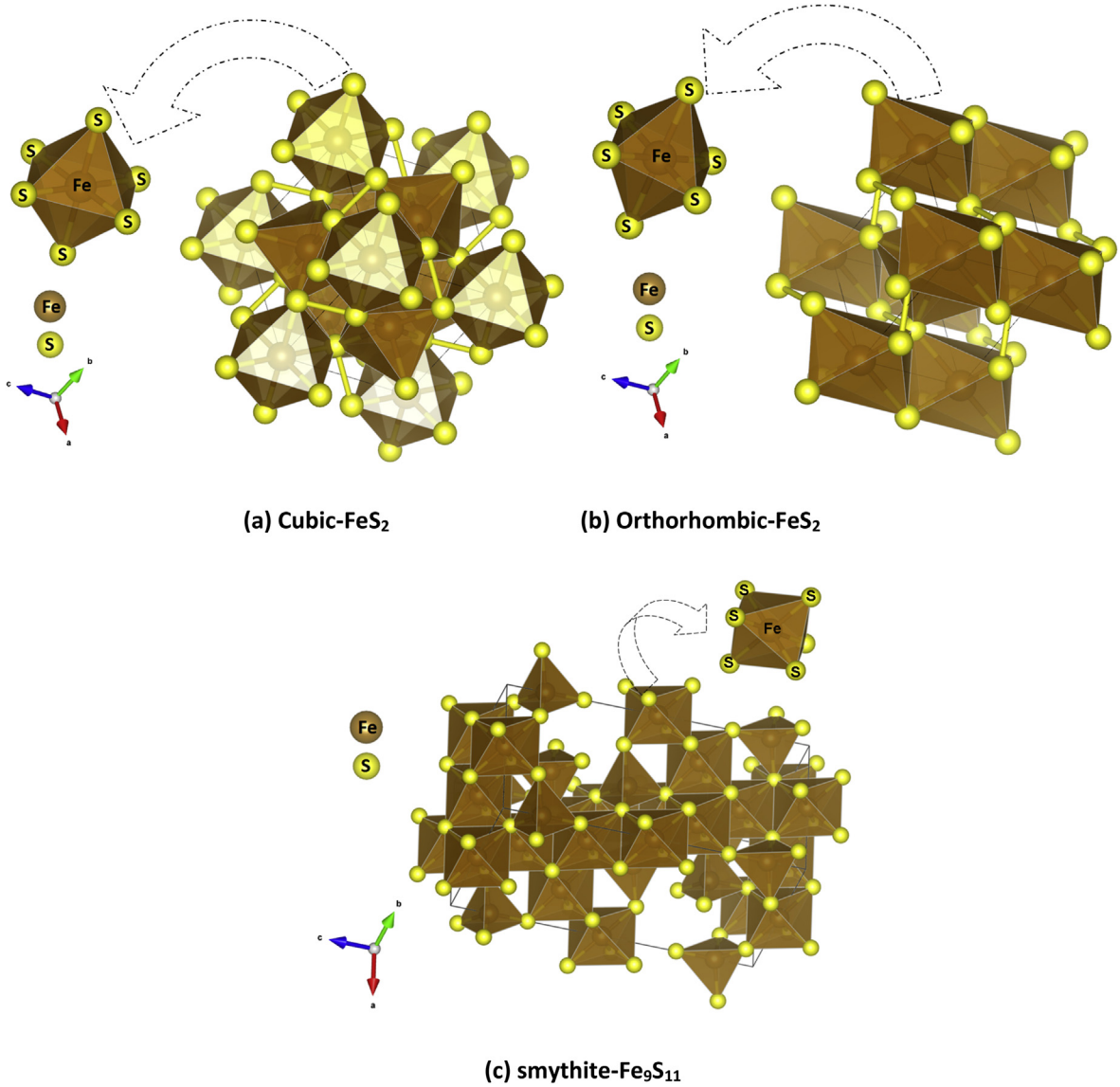

Fig. 2. The crystal structure of the relaxed geometry for cubic- FeS_2 (a), orthorhombic-FeS_2 (b) and smythite Fe_9S_{11} (c). The octahedron (FeS_6) is formed by the coordination of Fe with the six S atoms. Each Fe atom is surrounded by six S atoms. The octahedrons are joined together through corner-sharing of an S atom.

heterogeneous composition with S/Fe atomic percent ratio varies from 1:1 up to 1:2. These values indicate that some decomposition of FeS took place. The incongruent element distribution can be caused by charge- or energy-inhomogeneous flowing of colliding FeS_{1-x} species.

The X-ray diffraction analysis of the commercial FeS sample allows the estimation of the relative amounts of crystalline constituents of this sample as troilite (~63%), pyrrhotite (~24%) and alpha-Fe (13%) [29]. Electron diffraction was used for the designation of the phase composition of the samples.

The electron diffraction (Fig. 4 A) of FeS deposit on Ta substrate reveals the presence of stable cubic pyrite (JCPDS file 00-001-1295) phase which is consistent with HRTEM analyses. The HRTEM image (Fig. 4 B) reveals partially crystallized film where nanosized crystal objects exhibit interlayer spacing d = 0.192 nm which corresponds with cubic pyrite interplanar distance 220, according to JCPDS PDF 00-001-1295. From the HRTEM images is visible that the deposit contains many 3-5 nm-sized nanocrystals surrounded by the amorphous phase. We can conclude that the interaction of ablated FeS particles with the unheated Ta surface, which is generally considered as an inert substrate, results to phase transformation of initial crystalline constituents of this sample as troilite (~63%), pyrrhotite (~24%) and alpha-Fe (13%) to stable cubic pyrite and less stable amorphous FeS phase.

The FeS ablative deposition on aluminium substrate leads to the formation of two crystalline phases along the amorphous matrix. Electron diffraction (Fig. 5) reveals that the deposit consists of stable FeS_2 cubic pyrite (01-1295) and, interestingly, of unstable Fe_9S_{11} rhombohedral smythite phase (JCPDS 10-0437). HRTEM images (Fig. 6 A, B) confirm above mentioned phases by detected interlayer spacing d = 0.245 nm (018) and d = 0.270 nm (200) which corresponds with smythite phase and pyrite phase, respectively.

FeS pulsed laser deposition on copper substrate results in the generation of highly multiphase structure consists of FeS_2 cubic pyrite, unstable Fe_9S_{11} rhombohedral smythite (JCPDS 10-0437), FeS_2 orthorhombic marcasite (JCPDS 00-003-0799) and amorphous phase. The presence of the three crystalline phases demonstrates electron diffraction which is given in Fig. 7 and HRTEM analyses (Fig. 8) showing d = 0.258 nm and d = 0.169 nm interlayer spacing which agrees with rhombohedral smythite (107) and orthorhombic marcasite phase (002), respectively.

Summary of phases obtained via laser induced phase transformation is given in Table 1. Achieved data reveal different phase composition on various substrates.

In contrary to our previous study [29] no reactive deposition and formation of intermetallics such as copper sulfides has been detected. The reason for different phase transformations and interactions consists in different wavelength (944.19 cm^{-1}), energy (1.4 J) and duration (a full width at half maximum of 150 ns) of the previously used laser.

We suggest that the higher-energy irradiation with longer pulse duration of TEA CO_2 laser resulted in interactions of colliding FeS_{1-x} particles and clusters and served as a driving force for the $FeS_{1-x}Cu$ interdiffusion and crystalline sulfidic phase formation, while actual above described parameters of irradiation have been proved to be favorable for phase conversion to stable and **unstable crystalline phases** along the amorphous phase.

Generally, smythite occurs as a low-temperature oxidation product of monoclinic pyrrhotite, and does not appear to be stable above 75 °C (e.g. ref. [34]). Marcasite converts to pyrite when heated under vacuum to temperatures in excess of ~400 °C [35]. Similar behaviour is observed at high pressures (~3.7 GPa) [36]. Metastable behaviour of marcasite with respect to pyrite is demonstrated also in the study [37] where irreversible inversion of fine grained marcasite to pyrite even at ambient temperatures has been reported. Pyrite is commonly considered as potentially useful photovoltaic and photoelectrochemical semiconductor. However, in contrary to previous works [38], similar band gap values for both pyrite and marcasite were determined. Band gaps of pyrite and marcasite have been recently reported as Eg ~0.95 eV and Eg ~0.85 eV, respectively [39]. This information makes marcasite a promising candidate for photovoltaic and photoelectrochemical application or designate this contaminant of pyrite as contributing to reduced band gap energy of the photovoltaic material. Moreover, marcasite compared to pyrite has been found as more reactive agent for microbiological and chemical oxidation which is affected by structural and thermodynamic differences between the two phases [40].

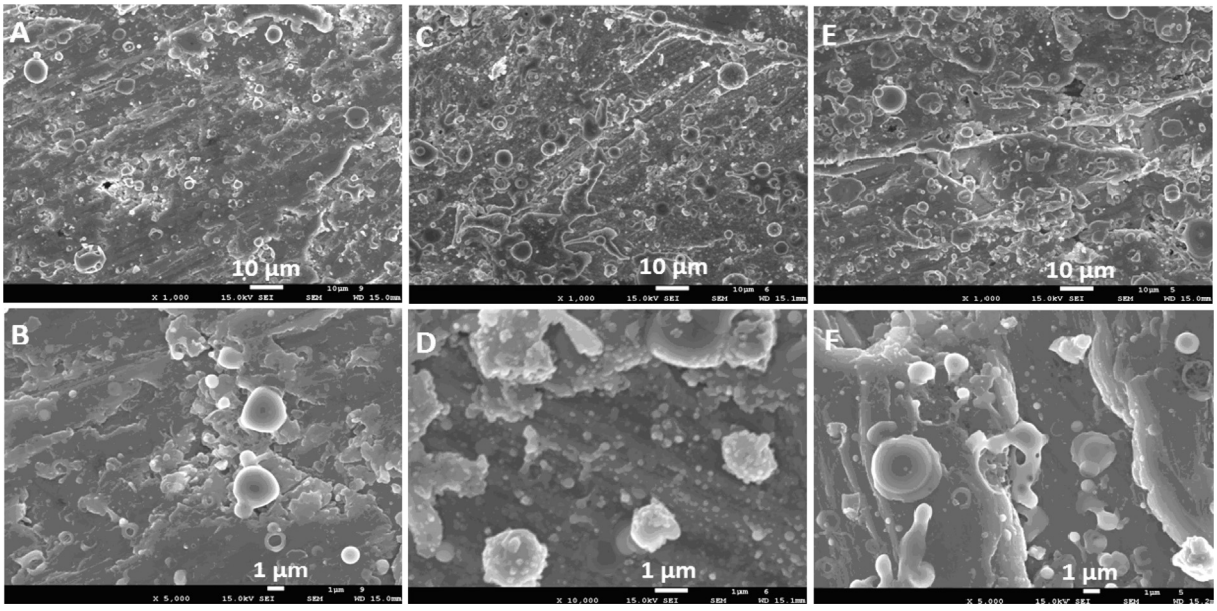

Fig. 3. Morphology of FeS deposits on (A,B) aluminium, (C,D) copper, (E,F) tantalum substrate.

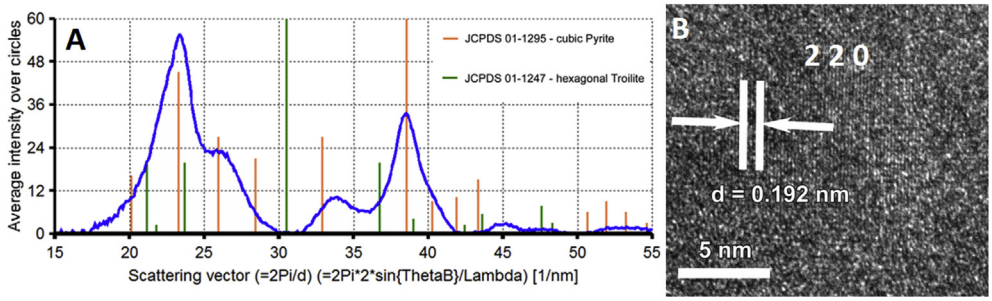

Fig. 4. (A) Electron diffraction of FeS deposit on Ta substrate, (B) HRTEM image of FeS deposit on Ta substrate depicting cubic pyrite FeS_2 phase.

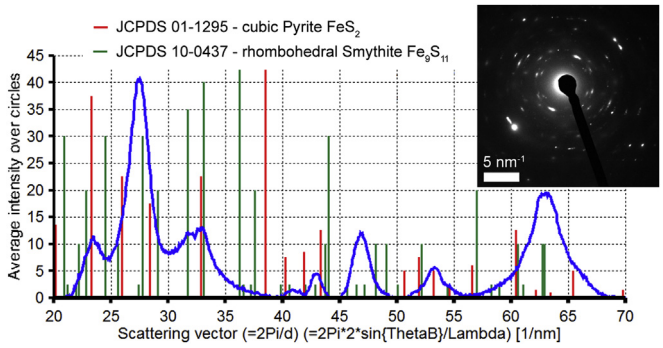

Fig. 5. Electron diffraction of FeS deposit on Al substrate.

phases as well as the smythite Fe_9S_{11} in Fig. 9a–c. It is clear that all phases exhibit indirect band gap of about 0.95 eV (cubic), 0.85 eV (orthorhombic) and 0.90 eV (smythite Fe_9S_{11}) which is in good agreement with the experimental data [39]. We should emphasize that the conduction band minimum (CBM) of the cubic phase is located at Γ point of the BZ and the valence band maximum (VBM) is situated between Γ and X points and the orthorhombic phase show the CBM at T point and the VBM between Γ and Z points. While for the smythite Fe_9S_{11} the CBM is located at F point and the VBM at Γ point. To obtain further insight into the type of states associated with each orbital of FeS_2 in cubic and orthorhombic phases, the projected density of states (DOS) is calculated. The angular momentum character of various structures in FeS_2 for the cubic and orthorhombic phases can be obtained by calculating the

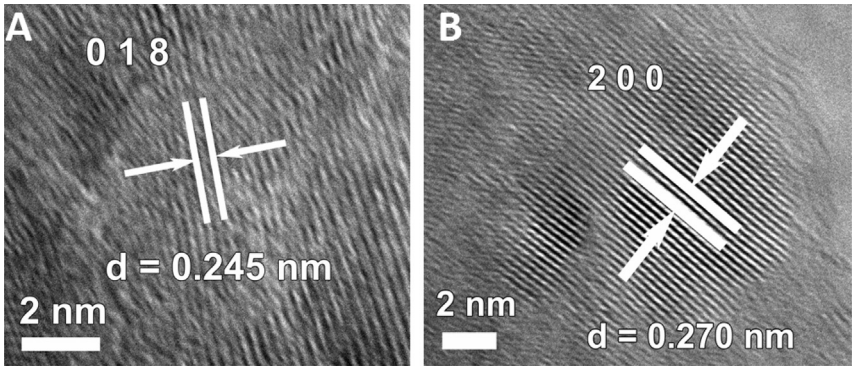

Fig. 6. HRTEM image of FeS deposit on Al substrate depicting (A) unstable Fe_9S_{11} rhombohedral smythite, (B) cubic pyrite FeS_2 phase.

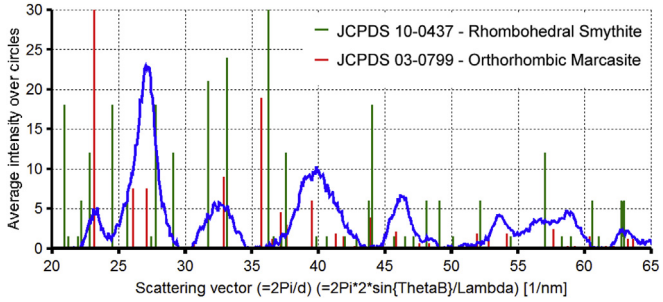

Fig. 7. Electron diffraction of FeS deposit on Cu substrate.

3.2. DFT calculations

The DFT results show the calculated electronic band structure along the high symmetry points for FeS_2 in cubic and orthorhombic

angular momentum projected density of states (PDOS), as shown in Fig. 10(a–f). It is demonstrated that moving from cubic to orthorhombic phase causes a significant changes in the dispersions of the Fe-4s/3p/4d and S-3s/3p states. It has been noticed that with moving from cubic to orthorhombic phase the Fe-dx^2y^2+dxy and Fe-dxz + dyz states in the cubic phase are split into Fe-dx^2y^2, Fe-dxy, Fe-dxz and Fe-dyz in the orthorhombic phase. It is clear that in the cubic (orthorhombic) phases the Fe-4s/3p/4dx^2y^2+dxy, Fe-4dxz + dyz and S-3s/3p (Fe-4s/3p/4dx^2y^2, Fe-4dxy, Fe-4dxz, Fe-4dyz and S-3s/3p) orbitals are distributed in the valence and conduction bands along the whole energy scale and show there exists a strong hybridization between the states. The hybridization degree favours enhancing the covalent bonding [41]. To support this statement we have calculated the valence band electronic charge density distribution of FeS_2 in cubic and orthorhombic phases.

To visualize the charge transfer and the chemical bonding characters, the valence band electronic charge density distribution are calculated and analyzed in details. Fig. 11(a–g) illustrated the

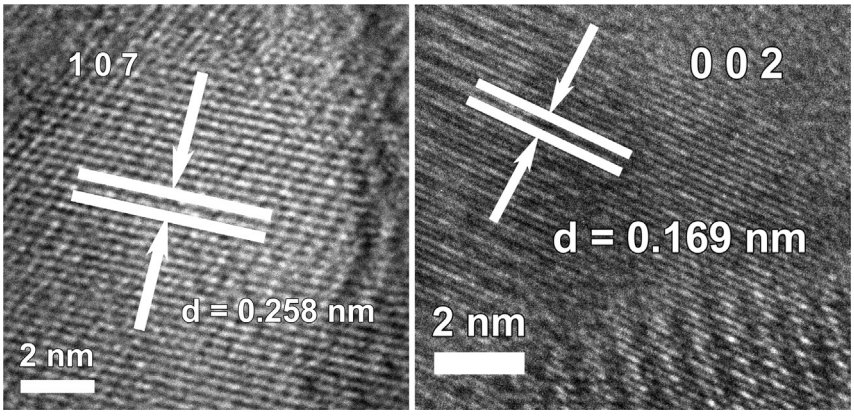

Fig. 8. (A) HRTEM image of FeS deposit on Cu substrate depicting (A) unstable Fe_9S_{11} rhombohedral smythite, (B) FeS_2 orthorhombic marcasite phase (002).

Table 1
List of obtained phase compositions of ablated FeS deposits on selected metal substrates.

Initial crystalline constituents of FeS irradiated target	Troilite (~63%), pyrrhotite (~24%) and alpha-Fe (13%)		
Used substrate	Ta	Al	Cu
Phase composition of the deposits	- stable cubic pyrite FeS_2 - amorphous phase	- unstable Fe_9S_{11} rhombohedral smythite - stable cubic pyrite FeS_2 - amorphous phase	- unstable Fe_9S_{11} rhombohedral smythite - metastable FeS_2 orthorhombic marcasite, - stable cubic pyrite FeS_2 - amorphous phase

calculated total valence charge density distribution in two crystallographic planes along the (1 0 0) and (1 0 1) directions for the three phases. According to Pauling scale the electro-negativity of Fe and S atoms are 1.83 and 2.58, respectively. Thus the electro-negativity differences between the atoms is small, therefore, the small electro-negativity differences indicating there exists covalent bonds [42,43]. Covalent bonding is more favourable for the transport of the carriers than ionic one [44]. The electronic charge density distribution plots show that the charge localizes mainly between Fe and the neighbouring S atoms indicating a strong covalent bonding. Also, due to the electro-negativity differences between Fe and S atoms, some valence electrons are transferred towards S atoms as it is clear that the S atoms are surrounded by uniform blue spheres which indicate the maximum charge accumulation according to thermoscale (Fig. 11(g)). We would like to highlight that the crystallographic plane along the (1 0 0) direction for the cubic phase and smythite Fe_9S_{11} shows only Fe atoms while for the orthorhombic phase it shows both Fe and S atoms and a cross section of the octahedron (FeS_6). The crystallographic plane along (1 0 1) direction show all atoms and a cross section of the

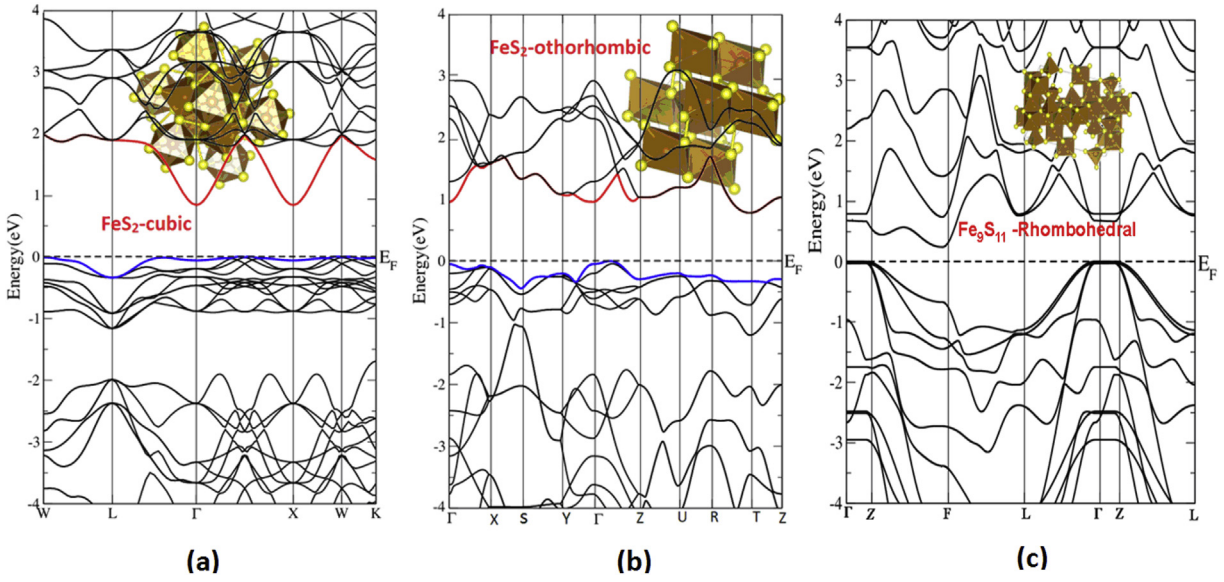

Fig. 9. The calculated electronic structure for the cubic (a), orthorhombic (b) and smythite Fe_9S_{11} (c).

octahedron (FeS_6). Therefore, the calculated valence band's electronic charge density distribution helps to gain deep insight into the nature of the chemical bonding, anisotropy in bonding and to explore the transport of the carriers.

4. Conclusions

Near-IR laser ablation of ferrous sulfide on Ta, Al, and Cu surfaces has been carried out and the thin films were characterized. Morphology of obtained homogeneous, dark, metallic coat consists of round-shaped and ring-like micro-particles with the similar heterogeneous composition with S/Fe atomic percent ratio spanning from 1:1 up to 1:2.

HRTEM and electron diffraction has been used for characterization of laser induced phase transformation of original FeS target and confirmed stable cubic pyrite phase (FeS_2) on Ta, Cu and Al substrate, metastable rhomboedric smythite Fe_9S_{11} on Al and Cu substrate and metastable orthorhombic marcasite (FeS_{2m}) on Cu substrate. All crystalline phases were shown in form of nanograins embedded in the amorphous matrix. This first example of ablative deposition of unstable FeS phases can encourage more investigation which can reveal interesting yet unknown properties of such structures. Furthermore, to gain deep insight into the electronic structure of the FeS_2 in cubic and orthorhombic phases and the smythite Fe_9S_{11}, the electronic band structure, the angular momentum character of various structures and the electronic charge

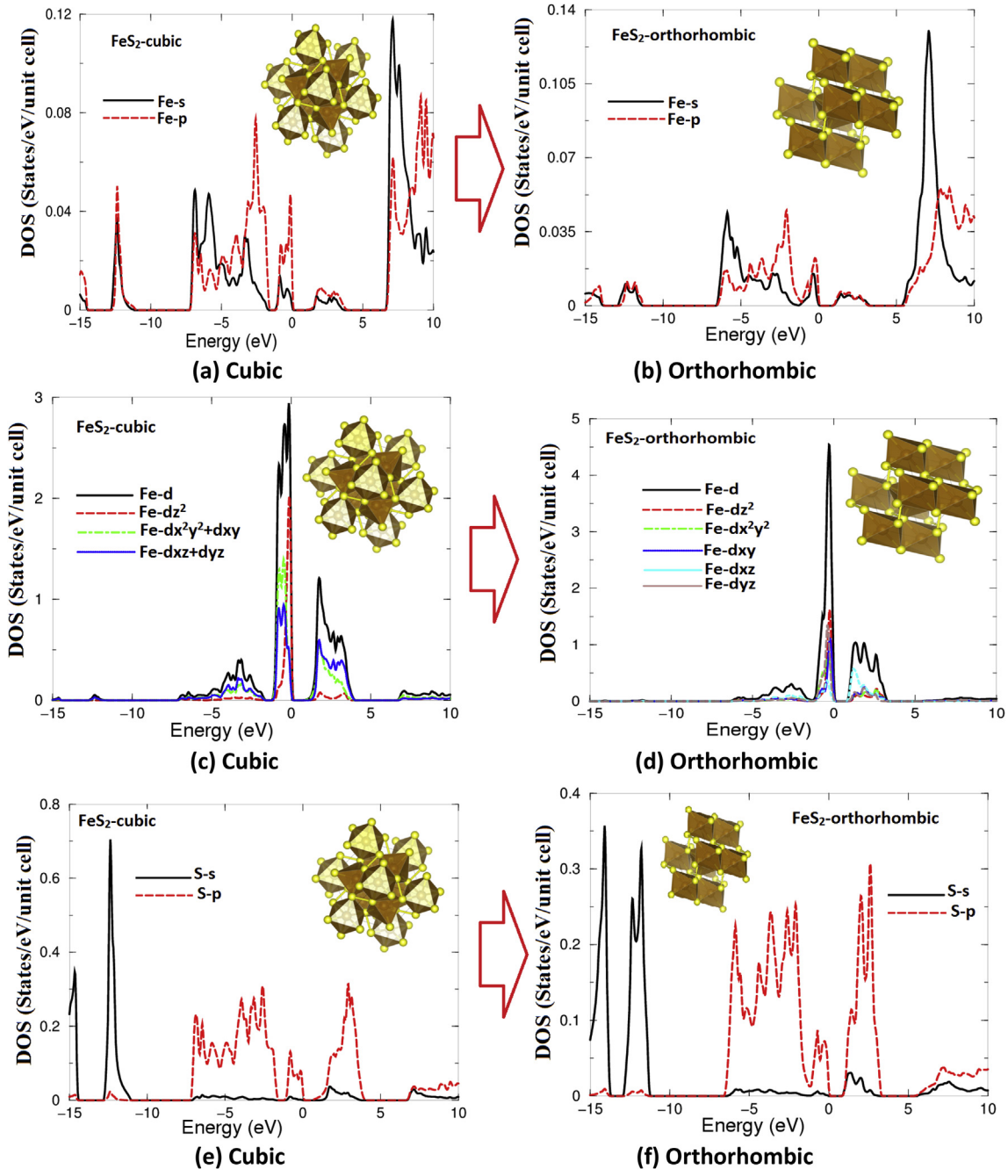

Fig. 10. Calculated angular momentum character of various structures in FeS_2 for the cubic and orthorhombic phases.

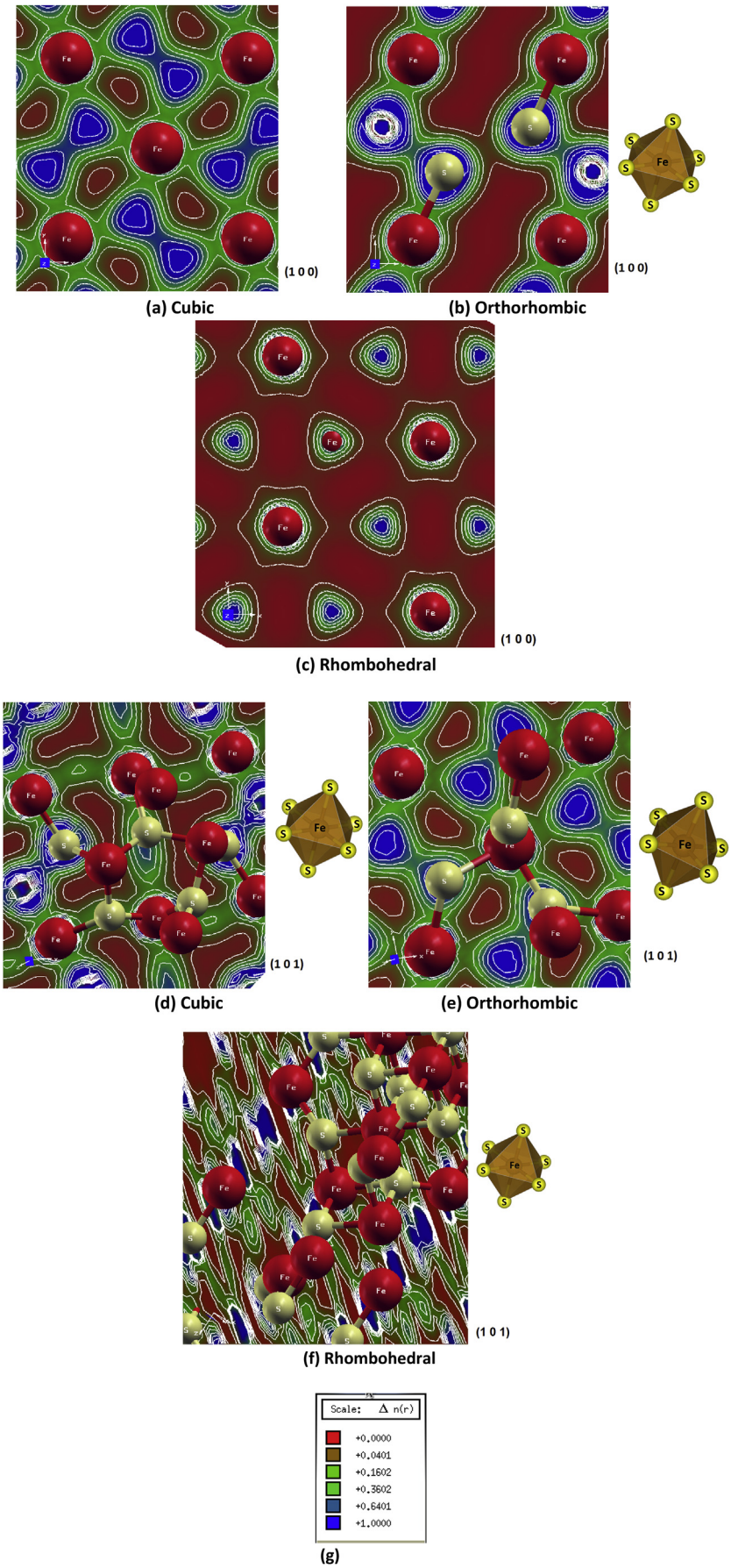

Fig. 11. The electronic charge density distribution in FeS_2 for the cubic and orthorhombic phases, and smythite Fe_9S_{11}.

density distribution are calculated based on the DFT calculations. Calculations show that a band gap reduction occurs with moving from cubic to orthorhombic phase and the orientation of the net local dipole moment direction of the octahedron changes to the opposite direction. The angular momentum character and the electronic charge density distribution reveal that there exists strong covalent bonding and some valence electrons are transferred towards S atoms.

Acknowledgements

The result was developed within the CENTEM project, reg. no. CZ.1.05/2.1.00/03.0088, cofunded by the ERDF as part of the Ministry of Education, Youth and Sports OP RDI programme and, in the follow-up sustainability stage, supported through CENTEM PLUS (LO1402) by financial means from the Ministry of Education, Youth and Sports under the National Sustainability Programme I. Computational resources were provided by MetaCentrum (LM2010005) and CERIT-SC (CZ.1.05/3.2.00/08.0144) infrastructures.

References

[1] W.K. Hofmann, M. Birkholz, Photoactive thin semiconducting iron pyrite prepared by sulfurization of iron oxides, Sol. Energy Mater. 20 (1990) 149–165.
[2] S.W. Lehner, K.S. Savage, J.C. Ayers, Vapor growth and characterization of pyrite (FeS_2) doped with Co, Ni, and As: variations in semiconducting properties, J. Cryst. Growth 286 (2006) 306–317.
[3] T. Takahashi, Magnetic properties of stoichiometric iron sulfide single crystals near the alpha transition temperature, Solid State Commun. 13 (9) (1973) 1335–1337.
[4] J.M. Soon, L.Y. Goh, K.P. Loh, Highly textured, magnetic $Fe_{(1+x)}S$ nanorods grown on silicon, Appl. Phys. Lett. 91 (2007) 084105–84111.
[5] D.J. Vaughan, A.R. Lennie, The iron sulphide minerals: their chemistry and role in nature, Sci. Prog. 75 (1991) 371 (Edinburgh).
[6] C.N.R. Rao, K.P.R. Pisharody, Transition metal sulfides, Prog. Solid State Chem. 10 (1975) 207.
[7] J.B. Goodenough, Structural chemistry of iron sulphide, Mater. Res. Bull. 13 (1978) 1305.
[8] V. Bessergenev, The use of complex compounds in chemical vapour deposition, J. Phys. Condens. Matter 16 (2004) S531.
[9] J.R. Gosselin, M.G. Townsend, R.J. Tremblay, Electric anomalies at the phase transition in FeS, Solid Stat. Commun. 19 (1976) 799.
[10] H. Nakazawa, N. Morimoto, Phase relations and superstructures of pyrrhotite, $Fe_{1-x}S$, Mater. Res. Bull. 6 (1971) 345.
[11] J.L. Horwood, M.G. Townsend, A.H. Webster, Magnetic susceptibility of single-crystal $Fe_{1-x}S$, J. Solid State Chem. 17 (1976) 35.
[12] A.S. Barnad, S.P. Russo, Shape and thermodynamic stability of pyrite FeS_2 nanocrystals and nanorods, J. Phys. Chem. 111 (31) (2007) 11742.
[13] M.J. Almond, H. Redman, D.A. Rice, Growth of thin layers of metal sulfides by chemical vapour deposition using dual source and single source precursors: routes to Cr_2S_3, α-MnS and FeS, J. Mater. Chem. 10 (2002) 2842.
[14] X. Ma, F. Xu, X. Wang, Y. Du, L. Chen, Z. Zhang, The U-shaped $Fe_{(1-x)}S$ microslots: growth, characterization, and magnetic property, J. Cryst. Growth 277 (2005) 314.
[15] M. Birkholz, D. Lichtenberger, C. Hoepfner, S. Fiechter, Sputtering of thin pyrite films, Sol. Energy Mater. Sol. Cells 27 (1992) 243.
[16] B. Rezig, H. Dalma, M. Kanzai, Iron pyrite FeS_2 for flexible solar cells, Renew. Energy 2 (1992) 25.
[17] G. Smestad, A. Da Silva, H. Tributsch, S. Fiechter, M. Kunst, N. Meziani, M. Birkholz, Formation of semiconducting iron pyrite by spray pyrolysis, Sol. Energy Mater. 18 (1989) 299.
[18] G. Smestad, E. Ennaoui, S. Fiechter, H. Tributsch, W.K. Hofman, M. Birkholz, Photoactive thin film semiconducting iron pyrite prepared by sulfurization of iron oxides, Sol. Energy Mater. 20 (1990) 149.
[19] B. Ouertani, J. Ouerfelli, M. Saadoun, B. Bessais, H. Ezzaouia, J.C. Bernede, Characterization of FeS 2-pyrite thin films synthesized by sulphuration of amorphous iron oxide films pre-deposited by spray pyrolysis, Mater. Charact. 54 (2005) 431.
[20] S. Bausch, B. Sailer, H. Keppner, G. Willeke, E. Bucher, G. Frommeyer, Preparation of pyrite films by plasma-assisted sulfurization of thin iron films, Appl. Phys. Lett. 25 (1990) 57.
[21] B. Thomas, T. Cibik, C. Hoepfner, D. Diesner, G. Ehlers, S. Fiechter, K. Ellmer, Formation of secondary iron-sulphur phase during the growth of polycrystalline iron pyrite (FeS_2) thin films by MOCVD, J. Mater. Sci. 9 (1998) 61.
[22] D.M.H. Schleigh, S.W. Chang, Iron pyrite and iron marcasite thin films prepared by low pressure chemical vapor deposition, J. Cryst. Growth 112 (1991) 737.
[23] I.J. Ferrer, C. Sanchez, Characterization of FeS_2 thin films prepared by thermal sulfidation of flash evaporated iron, J. Appl. Phys. 70 (1991) 2641.
[24] A. Ennaoui, G. Schlichtlorel, S. Fiechter, H. Tributsch, Vapor phase epitaxial growth of FeS2 pyrite and evaluation of the carrier collection in a liquid-junction solar cell (PEC), Sol. Energy Mater. Sol. Cells 25 (1992) 169.
[25] P.P. Chin, J. Ding, J.B. Yi, B.H. Liu, Synthesis of FeS 2 and FeS nanoparticles by high-energy mechanical milling and mechanochemical processing, J. Alloys Compd. 390 (2005) 255.
[26] D.B. Chrisey, G.K. Hubler, Wiley-interscience, Pulsed Laser Deposition of Thin Films, 1994. New York.
[27] D. Geohegan, M. Stuke, Fogarassy, laser ablation, in: MRS Symp. Proc., vol. 55, Elsevier Amsterdam, 1995.
[28] D. Yokoyma, K. Namiki, Y.J. Yamada, Mössbauer study of Fe/S and Fe/O films produced by laser ablation of pyrite and hematite, Radioanal. Nucl. Chem. 268 (2006) 283.
[29] M. Urbanova, D. Pokorna, P. Bezdička, J. Kupčik, T. Křenek, Reactive deposition of laser ablated FeS_{1-x} particles on a copper surface, RSC Adv. 4 (2014) 11543–11551.
[30] J.L. Lábár, Consistent indexing of a (set of) SAED pattern(s) with the Process Diffraction program, Ultramicroscopy 103 (2005) 237–249.
[31] P. Blaha, K. Schwarz, G.K.H. Madsen, D. Kvasnicka, J. Luitz, WIEN2k, An Augmented Plane Wave Plus Local Orbitals Program for Calculating Crystal Properties, Vienna University of Technology, Austria, 2001.
[32] J.P. Perdew, K. Burke, M. Ernzerhof, Generalized gradient approximation made simple, Phys. Rev. Lett. 77 (1996) 3865–3868.
[33] F. Tran, P. Blaha, Accurate band gaps of semiconductors and insulators with a semilocal exchange-correlation potential, Phys. Rev. Lett. 102 (2009) 226401.
[34] M.E. Fleet, Synthetic smythite and monoclinic Fe_3S_4, Phys. Chem. Miner. 8 (1982) 241–246.
[35] M.E. Fleet, Structural aspects of marcasite-pyrite transformation, Can. Mineral. 10 (1970) 225–231.
[36] V.K. Gudelli, V. Kanchana, S. Appalakondaiah, G. Vaitheeswaran, M.C. Valsakumar, Phase stability and thermoelectric properties of the mineral FeS_2: an Ab initio study, J. Phys. Chem. C 117 (41) (2013) 21120–21131.
[37] J.B. Murowchick, H.L. Barnes, Marcasite precipitation from hydrothermal solution, Geochim. Cosmochim. Acta 50 (1986) 2615–2629.
[38] I. Dódony, M. Pósfai, P.R. Buseck, Structural relationship between pyrite and marcasite, Am. Mineral. 81 (1–2) (1996) 119–125.
[39] C. Sánchez, E. Flores, M. Barawi, J.M. Clamagirand, J.R. Ares, I.J. Ferrer, Marcasite revisited: optical absorption gap at room temperature, Solid State Commun. 230 (2016) 20–24.
[40] H. Wang, J.M. Bigham, O.H. Tuovinen, Oxidation of marcasite and pyrite by iron-oxidizing bacteria and archaea, Hydrometallurgy 88 (2007) 127–131.
[41] A.H. Reshak, Z.A. Alahmed, J. Bila, V.V. Atuchin, B.G. Bazarov, O.D. Chimitova, M.S. Molokeev, I.P. Prosvirin, A.P. Yelisseyev, Exploration of the electronic structure of monoclinic α-$Eu_2(MoO_4)_3$: DFT-Based study and x-ray photoelectron spectroscopy, J. Phys. Chem. C 120 (19) (2016) 10559–10568.
[42] Schlusseltechnologien Key Technologies, 41st IFF Springschool, 2010, pp. A1–A18.
[43] S. Khan, A.H. Reshak, Linear, nonlinear optical susceptibilities, hyperpolarizability, and space electronic charge density of meso silver(I) histidinate [Ag(D-his)]n (Hhis = histidine), Polyhedron 85 (2015) 962–970.
[44] F. Wu, H.Z. Song, J.F. Jia, X. Hu, Effects of Ce, Y, and Sm doping on the thermoelectric properties of Bi_2Te_3 alloy, Prog. Nat. Sci. Mater. Int. 23 (4) (2013) 408–412.